

Synthesis, disorder and Ising anisotropy in a new spin liquid candidate $\text{PrMgAl}_{11}\text{O}_{19}$

Yantao Cao^{1,2}, Huanpeng Bu², Zhendong Fu², Jinkui Zhao^{2,3}, Jason S. Gardner^{4,*}, Zhongwen Ouyang⁵, Zhaoming Tian^{5,†}, Zhiwei Li^{1,‡}, and Hanjie Guo^{2,§}

¹Key Lab for Magnetism and Magnetic Materials of the Ministry of Education, Lanzhou University, Lanzhou 730000, China

²Songshan Lake Materials Laboratory, Dongguan, Guangdong 523808, China

³Institute of Physics, Chinese Academy of Sciences, Beijing 100190, China

⁴Materials Science and Technology Division, Oak Ridge National Laboratory, Oak Ridge, Tennessee 37831, USA

⁵School of Physics and Wuhan National High Magnetic Field Center, Huazhong University of Science and Technology, Wuhan 430074, P. R. China.

*gardnerjs@ornl.gov

†tianzhaoming@hust.edu.cn

‡zweili@lzu.edu.cn

§hjguo@sslslab.org.cn

ABSTRACT

Here we report the successful synthesis of large single crystals of triangular frustrated $\text{PrMgAl}_{11}\text{O}_{19}$ using the optical floating zone technique. Single crystal X-ray diffraction measurements unveiled the presence of quenched disorder within the mirror plane, specifically $\sim 7\%$ of Pr ions deviating from the ideal $2d$ site towards the $6h$ site. Magnetic susceptibility measurements revealed an Ising anisotropy with the c -axis being the easy axis. Despite a large spin-spin interaction that develops below ~ 10 K and considerable site disorder, the spins do not order or freeze down to at least 50 mK. The availability of large single crystals offers a distinct opportunity to investigate the exotic magnetic state on a triangular lattice with an easy axis out of the plane.

Keywords: spin liquid, disorder, frustration, triangular lattice, Ising anisotropy

Introduction

Quantum spin liquids (QSLs) represent an intriguing state where the spins remain disordered even at zero Kelvin due to quantum fluctuations, albeit with strong spin-spin couplings¹. Achieving a QSL ground state is challenging because of the propensity for the spin sublattice to freeze as the temperature is lowered, especially around defects and/or disorder which act as pinning centers. For example, in the triangular lattice of YbMgGaO_4 , the presence of site disorder between the nonmagnetic ions Mg and Ga induces a spin glass behavior². However, disorder is not always detrimental to the QSL state. Studies on the pyrochlore oxides^{3,4} and $1T\text{-TaS}_2$ ⁵ reveal that the quenched disorder does not compete, but rather cooperates with the frustration to induce strong quantum fluctuations, and may give rise to emergent spin disordered state responsible for the gapless excitations.

From an experimental point of view, a QSL state does not break any symmetry making it arduous to identify using a single technique⁶. Inelastic neutron scattering plays an important role in providing crucial evidence for a QSL state, as fractional excitations, such as spinons, manifest as a distinctive excitation continuum in the spectrum⁷. The availability of high-quality large single crystals is essential for neutron scattering due to the small scattering cross-section and low neutron flux. Similar requisites hold true for other measurements, such as spin thermal transport, to minimize any grain boundary effects as well as the anisotropic characterizations of magnetic behaviors^{8,9}.

Here we present the single crystal growth of a hexaaluminate, $\text{PrMgAl}_{11}\text{O}_{19}$, using the optical floating zone technique. Crystal growth and basic magnetic property measurements on this series of lanthanide aluminates have been reported^{10,11}, but a detailed characterization down to millikelvin is still lacking. Our previous results on the isostructural, polycrystalline $\text{PrZnAl}_{11}\text{O}_{19}$ already suggested the magnetic sublattice of Pr^{3+} ions, decorating a triangular lattice, has the potential to host a Dirac QSL^{12,13}. The triangular network of Pr ions reside within the ab plane, and are connected via intermediate O ions which are also within the triangular plane, forming a nearly linear Pr-O-Pr bond with an angle of about 176.7° . These layers

are separated along the c -axis by ~ 11 Å while the nearest neighbor Pr-Pr bond is ~ 5.59 Å; see Fig. 1. As a comparison, the distance between triangular layers in YbMgGaO₄ are about 8 Å with a nearest neighbor bond length of ~ 3.40 Å¹⁴. Moreover, the large difference in the ionic radii between the magnetic and nonmagnetic ions inhibits any site mixing between the magnetic and nonmagnetic ions. These structural features indicate that this system is an ideal quasi-two-dimensional system free from chemical disorder, and great starting conditions for realizing the QSL state. Indeed, the signature of forming a QSL state has been observed in ac susceptibility measurements of PrZnAl₁₁O₁₉ revealing no spin freezing or ordering down to 50 mK, despite a considerable antiferromagnetic coupling strength of about -9 K. In addition, inelastic neutron scattering exhibits an abnormal broadening of low energy excitations at ~ 1.5 meV¹³. Unfortunately single crystals of PrZnAl₁₁O₁₉ are currently not available at the size needed for inelastic neutron scattering.

By substituting Zn with the less evaporative Mg element, we have succeeded in growing sizable single crystals of PrMgAl₁₁O₁₉ suitable for neutron scattering measurement. However, we have identified site disorder within the mirror plane, with about 7% of the Pr ions displaced from the ideal position. Magnetic susceptibility measurements show the moments lying perfectly along the c -axis (or perpendicular to the triangular plane) and do not freeze down to 50 mK. We argue that the system keeps fluctuating despite strong couplings and site disorder, which makes this system unique for a triangular system with Ising character.

1 Methods

Polycrystalline samples were prepared using a standard solid-state reaction technique. Raw materials of Pr₆O₁₁ (99.99%), MgO (99.99%), and Al₂O₃ (99.99%) were dried at 900°C over night prior to reaction to avoid moisture contamination. Then, stoichiometric amounts of the raw materials were mixed and ground thoroughly, pressed into pellets and sintered at 1400°C \sim 1600°C with several intermediate grindings. The powder sample was mixed with about 1% \sim 2% excess of MgO and pressed into a cylindrical rod of ~ 6 mm in diameter and ~ 140 mm (~ 35 mm) in length as a feed (seed) rod using a hydrostatic pressure of 70 MPa. The obtained feed and seed rods were sintered at 1500°C for 2 hours. Subsequent single crystal growth was conducted in an optical floating zone furnace (HKZ300) in pure argon atmosphere at 10 bar. After floating zone growth, the several-centimeter-sized as-grown crystal was annealed at 1000°C in flowing O₂ for 24 hours and then slowly cooled down to room temperature in order to avoid any possible oxygen vacancy.

The single crystal X-ray diffraction (XRD) measurement was performed on a XtaLAB Synergy diffractometer (Rigaku) at room temperature using the Mo- K_α radiation. The experimental conditions are tabulated in Tab. 1. Part of the single crystal was crushed into powders for powder XRD measurement performed on a MiniFlex diffractometer (Rigaku) with the Cu- K_α radiation. JANA¹⁵ and FULLPROF¹⁶ packages were used for crystal structure refinement.

Heat capacity measurements were carried out on the Physical Property Measurement System (PPMS, Quantum Design) equipped with a dilution insert using the relaxation method. The DC magnetic susceptibility between 2 and 350 K was measured using the vibrating sample magnetometer (VSM) option of the PPMS. The AC magnetic susceptibility between 0.05 and 15 K was measured using the ACMS-II and ACDR options of the PPMS. For the AC susceptibility measurement, a driven field of 1-3 Oe in amplitude was used.

2 Results

The single crystal growth was initially attempted in a pure oxygen atmosphere, which turns out to be unstable and results in cavities along the as-grown crystals. This occurrence indicates the dissolution of oxygen in the melt, forming stable bubbles during the growth process. Therefore, subsequent growths were performed in a pure Ar atmosphere at 10 bar pressure in order to minimize the evaporation of the Mg element. The upper and lower rods were counter-rotated at a rate of 20 rpm, and moved downwards simultaneously at a rate of 2 mm/h. These conditions led to the successful growth of centimeter-sized single crystals, as depicted in the inset of Fig. 2(a). The single-domain nature was confirmed by Laue diffraction measurements along the rod. A typical Laue pattern is shown in Fig. 2(a) with the X-ray beam nearly parallel to the c -axis. Laue measurements also confirm that the crystal was grown along the a^* direction.

The quality of the single crystal was further characterized by X-ray diffraction of single crystals and crushed crystals. All peaks in the powder diffraction pattern can be indexed by the space group $P6_3/mmc$, indicating an impurity-free phase; see the Supplementary Materials (SM)¹⁷. The precession images within the HK0, 0KL, and H0L planes from the single crystal XRD measurements are shown in Fig. 2(b-d). The sharp peaks confirm the high quality of the crystal. The structure refinement is consistent with the findings reported by Kahn *et al.* for LaMgAl₁₁O₁₉¹¹. The final structure parameters extracted from the single crystal refinement are listed in Tab. 2. It was found that about 7% of the Pr ions at the 2d (Pr1) site were shifted about 0.6 Å away from the ideal position towards the 6h (Pr2) site. Moreover, within the mirror plane of the structure, the Al5 ion displayed an anomalous atomic displacement parameter (ADP) along the c -axis, U_{33} , which amounts to 0.018 Å², compared to the others of around 0.007 Å². Therefore, it is set to be slightly off the mirror plane with half occupancy at the

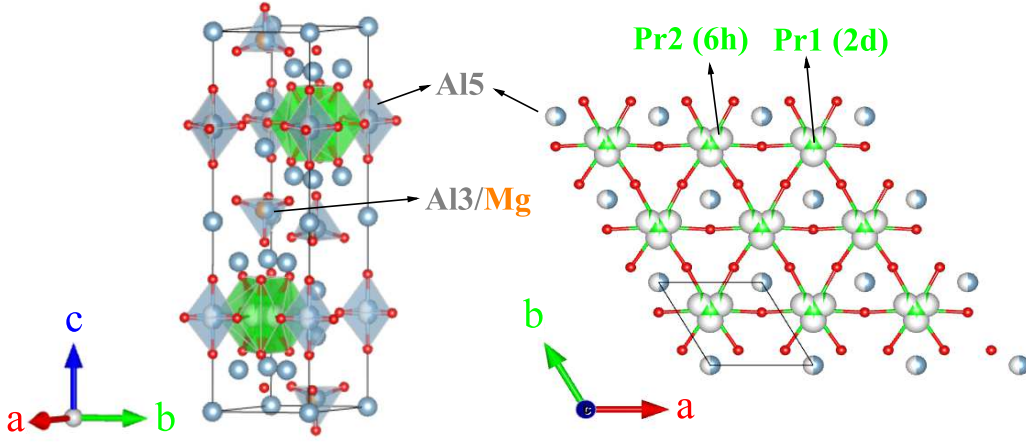


Figure 1. The crystal structure of $\text{PrMgAl}_{11}\text{O}_{19}$ extracted from single-crystal XRD refinement. Green - Pr; grey - Al; red - O; orange - Mg. The mirror plane including the disordered Pr ions is depicted in the right panel.

4e site. Note, that with the resolution of our lab-based powder X-ray diffractometer, this anomalous ADP would be within errors and not highlighted. The last unsolved issue is the occupied position of the Mg ions. It is difficult to distinguish Mg^{2+} from Al^{3+} by means of X-ray diffraction because of the same number of electrons for both ions. However, neutron powder diffraction measurement on its sister compound $\text{CeMgAl}_{11}\text{O}_{19}$ ¹⁸ indicated that Mg is likely positioned at the Al3 site with an AlO_4 tetrahedron coordination, which also shows an anomalous ADP if solely occupied by Al ions. Therefore, the Mg ions are mixed with the Al3 ion at the 4f site with 0.5 occupancy. The refined structure is shown in Fig. 1 and those particular ions are highlighted.

Moving to the magnetic property measurements. The X-ray photoelectron spectroscopy (XPS) measurements indicate a pure Pr^{3+} state¹⁷. Fig. 3(a) shows the temperature dependence of the magnetic susceptibility measured along different crystallographic directions. Note, that the c - and c^* -directions are identical. The data shows pronounced anisotropy behavior with the moment predominantly aligned along the c -axis. No difference between the zero-field-cooled (ZFC) and field-cooled (FC) curves can be observed, consistent with a dynamical (paramagnetic) state. The temperature dependence of χ_c^{-1} is shown in Fig. 3(b). A Curie-Weiss (CW) fit, $\chi_c^{-1} = (T - \theta_{\text{CW}})/C$, to the data above 250 K yields a positive Curie temperature θ_{CW} of 67 K. It should be noted that at these elevated temperatures we expect a large contribution from the crystal electric field (CEF) effect since two CEF levels were observed at ~ 12 and 35 meV¹³ in the isostructural $\text{PrZnAl}_{11}\text{O}_{19}$. At low temperatures where only the low-lying CEF ground state is occupied, the influence from the higher excitation levels is negligible, a CW-like fit then provides a measure of the intersite interactions. A fit below 10 K yields θ_{CW} of -8 K, indicating strong antiferromagnetic couplings; see Fig. 3(b). The effective moment is $5.18 \mu_B/\text{Pr}$, which is close to the expected value of $g_c^{\text{ESR}} \sqrt{S(S+1)} = 4.42 \mu_B/\text{Pr}$, where $g_c^{\text{ESR}} = 5.1$ is the g factor determined from ESR measurement¹⁷, and $S = 1/2$, implying that the low temperature magnetic properties are governed by an effective $S = 1/2$ state. AC susceptibility measurements along the c -axis show no sign of long-range ordering, nor any spin freezing down to 50 mK; see Fig. 3(c). The field dependence of isothermal magnetization (Fig. 3(d)) reveals negligible magnetization along the a^* direction compared to that of the c direction. It is about 20 times larger along the c axis at 2 K and 14 T, which can be easily explained by a slight misalignment (2 degrees) of the crystal during the measurement. Thus, the system can be considered as a well-defined Ising system.

In order to have more insights into the magnetic ground state, we performed CEF analysis and fit the CEF Hamiltonian to $\chi_c^{-1}(T)$. Although there are two inequivalent Pr sites, most of the Pr ions (> 90%) are still located at the 2d site with a D_{3h} symmetry. Thus, we start with a model disregarding the disorder effect at the Pr site. In such a case, the CEF Hamiltonian can be expressed as

$$\mathcal{H}_{\text{CEF}} = \sum_{n,m} B_n^m O_n^m, \quad (1)$$

where O_n^m are the Stevens operators, and only the CEF parameters B_2^0 , B_4^0 , B_6^0 and B_6^6 are nonzero. The presence of the O_6^6 term admixes those states $|J, m_J\rangle$ differ in m_J by 6. For Pr^{3+} , the total angular momentum number $J = 4$. Thus, there are three doublets: two are formed by a linear combination of $|\pm 4\rangle$ and $|\mp 2\rangle$, and the other is $|\pm 1\rangle$. The three singlets are consisting of $|3^a\rangle = 1/\sqrt{2}(|3\rangle + |-3\rangle)$, $|3^b\rangle = 1/\sqrt{2}(|3\rangle - |-3\rangle)$, and $|0\rangle$. Therefore, if the ground state is a doublet and

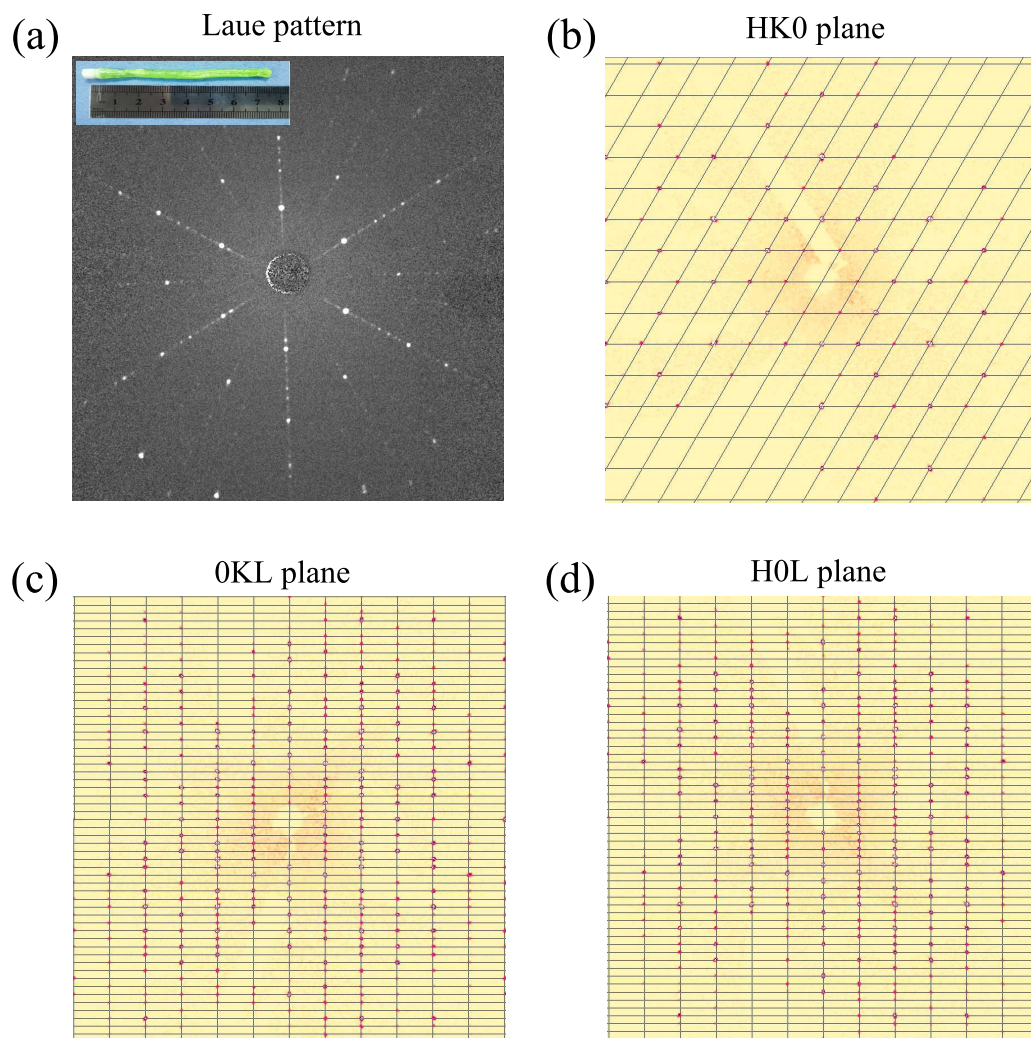


Figure 2. X-ray studies of $\text{PrMgAl}_{11}\text{O}_{19}$. (a) A Laue pattern with the X-ray beam approximately along the c axis. The inset shows a photo of the as-grown single crystal. (b-d) Precession images within the HK0, 0KL and H0L planes constructed from the single-crystal XRD measurements.

Table 1. Experimental conditions for the single crystal XRD measurements, and agreement factors for the refinement.

Formula	PrMgAl ₁₁ O ₁₉
Space group	<i>P</i> 6 ₃ / <i>mmc</i> (No. 194)
<i>a</i> , <i>b</i> (Å)	5.58700(10)
<i>c</i> (Å)	21.8732(6)
<i>V</i> (Å ³)	591.29(2)
<i>Z</i>	2
2 Θ (°)	3.72 - 82.16
No. of reflections, <i>R</i> _{int}	12534, 4.11%
No. of independent reflections	614
No. of parameters	48
Index ranges	-9 ≤ <i>H</i> ≤ 10, -10 ≤ <i>K</i> ≤ 10, -39 ≤ <i>L</i> ≤ 39
<i>R</i> , <i>wR</i> ₂ *	1.69%, 4.60%
Goodness of fit on <i>F</i> ²	1.42
Largest difference peak/hole (<i>e</i> /Å ³)	0.34/-0.38

*For a direct visualization of the fitting quality, see F_{obs}^2 vs. F_{cal}^2 in the SM¹⁷.

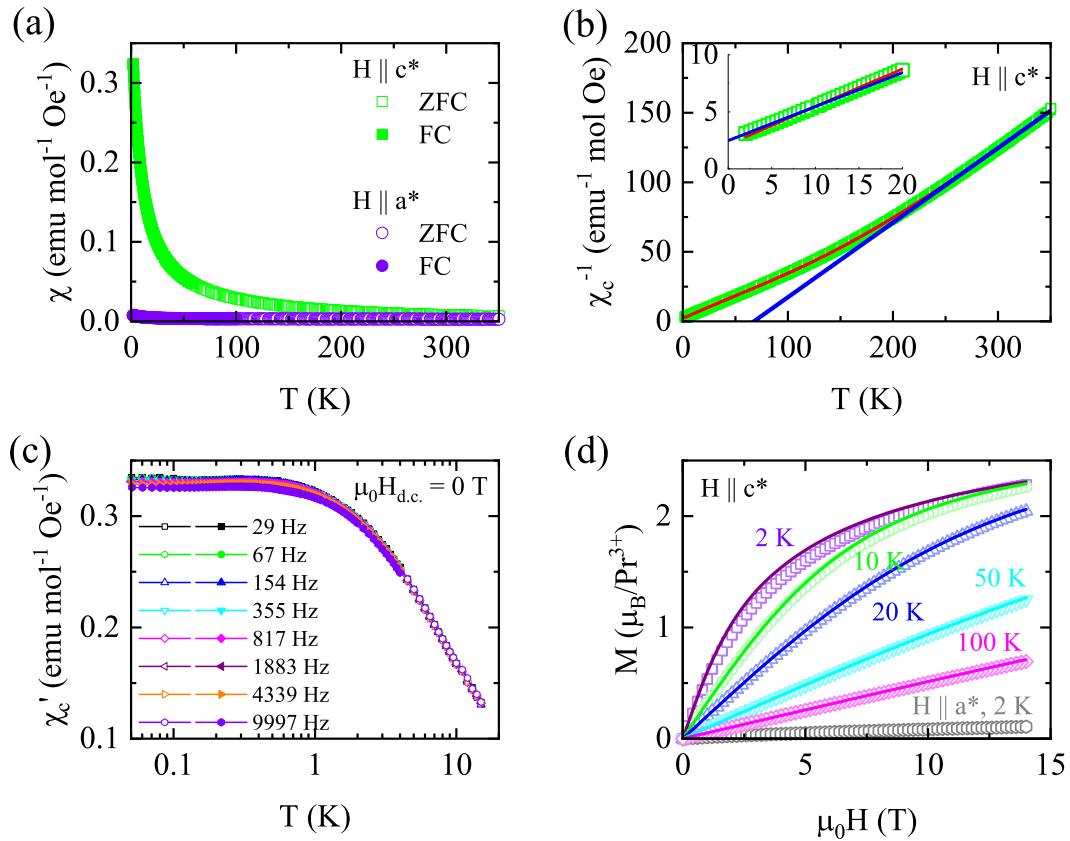


Figure 3. Temperature and field dependence of the dynamic susceptibility of PrMgAl₁₁O₁₉. (a) Temperature dependence of the magnetic susceptibility measured with the magnetic fields applied along the reciprocal *a** and *c** directions. (b) Temperature dependence of the inverse susceptibility, $\chi_c^{-1}(T)$. The red and blue curves are according to the CEF fit and Curie-Weiss fit, respectively. The inset highlights the low-temperature region. (c) Temperature dependence of the real component of the ac susceptibility, $\chi_c'(T)$, measured at various frequencies. (d) Isothermal magnetization measured at various temperatures. The solid lines represent the magnetization calculated from the CEF parameters.

Table 2. Refined crystal structure parameters.

Atom	occ.	x	y	z
Pr1 (2d)	0.928(10)	1/3	2/3	0.75
Pr2 (6h)	0.024(3)	0.271(5)	0.729(5)	0.75
Al1 (2a)	1	0	0	0
Al2 (4f)	1	1/3	2/3	0.18998(4)
Al3 (4f)	0.5	1/3	2/3	0.47275(4)
Mg (4f)	0.5	1/3	2/3	0.47275(4)
Al4 (12k)	1	0.16738(4)	0.33477(9)	0.60839(2)
Al5 (4e)	0.5	0	0	0.2428(3)
O1 (6h)	1	0.18122(15)	0.3624(3)	0.25
O2 (12k)	1	0.15214(11)	0.3043(2)	0.44609(6)
O3 (12k)	1	-0.0112(2)	0.49442(11)	0.34808(5)
O4 (4f)	1	1/3	2/3	0.55837(10)
O5 (4e)	1	0	0	0.34818(9)
Atom	U_{11}/U_{12} (Å ²)	U_{22}/U_{13} (Å ²)	U_{33}/U_{23} (Å ²)	
Pr1	0.0099(3)	0.0099(3)	0.00756(13)	
	0.00493(15)	0	0	
Pr2	0.030(5)	0.030(5)	0.019(4)	
	0.007(5)	0	0	
Al1	0.0070(3)	0.0070(3)	0.0078(5)	
	0.00352(14)	0	0	
Al2	0.0072(2)	0.0072(2)	0.0067(4)	
	0.00358(11)	0	0	
Al3/Mg	0.0068(2)	0.0068(2)	0.0076(4)	
	0.00340(12)	0	0	
Al4	0.00682(17)	0.0071(2)	0.0075(2)	
	0.00353(11)	-0.00007(7)	-0.00013(14)	
Al5	0.0069(3)	0.0069(3)	0.018(3)	
	0.00347(17)	0	0	
O1	0.0107(5)	0.0075(6)	0.0080(7)	
	0.0038(3)	0	0	
O2	0.0096(4)	0.0123(5)	0.0091(5)	
	0.0062(2)	0.00117(19)	0.0023(4)	
O3	0.0079(4)	0.0077(3)	0.0086(5)	
	0.0040(2)	0.0005(3)	0.00024(17)	
O4	0.0075(5)	0.0075(5)	0.0119(9)	
	0.0037(2)	0	0	
O5	0.0078(4)	0.0078(4)	0.0103(8)	
	0.0039(2)	0	0	

well separated from the first excited state, it will be highly anisotropic since $\langle J^\pm \rangle = 0$. To estimate the energy separation, we use the PyCrystalField package¹⁹ to fit \mathcal{H}_{CEF} to the magnetic susceptibility data. To do so, we calculate the magnetic susceptibility $\chi_{CEF}^c = M_{CEF}^c/H$ based on the CEF Hamiltonian, and treat the influence of the surrounding ions to a mean field level, so that $\chi_{cal}^c = \chi_{CEF}^c/(1 - \lambda\chi_{CEF}^c)$. By minimizing $\chi^2 = \sum_i (1/\chi_{cal,i}^c - 1/\chi_{obs,i}^c)^2$, the best fit yields $B_2^0 = -0.84181$ meV, $B_4^0 = -0.00516$ meV, $B_6^0 = -0.00012$ meV, $B_6^6 = -0.00602$ meV, and $\lambda = -1.19$ T/ μ_B . The eigenvectors and eigenenergies can be found in the SM¹⁷. The negative λ indicates an antiferromagnetic interaction among the spins. From $\lambda = zJ_c/(\mu_B gJ)^2$, where z is the number of nearest neighbors, the exchange constant J_c can be estimated as $\sim -0.73 \times 10^{-2}$ meV (-0.08 K). The small exchange constant is partly due to the large effective moment of Pr^{3+} ($J = 4$)²⁰. In the effective spin $S = 1/2$ picture, it will be enhanced by a factor of $\frac{J(J+1)}{S(S+1)} = 26.7$ (~ -2.1 K). Correspondingly, the Curie-Weiss temperature at low temperature can be estimated as $\theta_{CW}^{cal} = S(S+1)zJ_c/3k_B \sim -3$ K, which is roughly consistent with the experimental value. The calculated $(\chi_{cal}^c)^{-1}$ is shown in Fig. 3(b), which reproduces the overall data very well. Using the CEF parameters and λ , the calculated isothermal magnetization is shown in Fig. 3(d). Again, the calculated curves agree well with the experimental values. The small discrepancy below ~ 10 K may suggest the onset of spin-spin interactions. Moreover, the g factors corresponding to the ground state doublets amount to $g_{ab} = g_J \langle \mp | J^\mp | \pm \rangle = 0$ and $g_c = 2g_J \langle \pm | J_z | \pm \rangle = 5.6$, consistent with the Ising character as inferred from the susceptibility measurements. The calculated g_c is also close to the ESR result¹⁷. These good agreements indicate that the magnetic ground state is well captured by our CEF analysis, although the excited state may be overestimated.

Figure 4(a) shows the specific heat measurements for $\text{PrMgAl}_{11}\text{O}_{19}$ under various magnetic fields. A nonmagnetic sample $\text{LaMgAl}_{11}\text{O}_{19}$ was also measured as a comparison. A broad hump can be observed at ~ 4 K in the zero field data. With an increase in magnetic field, the peak is shifted towards high temperatures, reminiscent of the Schottky anomaly. However, upon subtracting the phonon contributions using $\text{LaMgAl}_{11}\text{O}_{19}$ as a reference sample, the magnetic component, C_m , can be obtained and shown in Fig. 4(b). It is apparent that C_m of $\text{PrMgAl}_{11}\text{O}_{19}$ does not exhibit a typical (multilevel, broadened) Schottky behavior^{21,22}, especially at the high temperature side where it displays a continuous increase up to 40 K. As a comparison, Fig. 4(d) shows the C_m of $\text{NdMgAl}_{11}\text{O}_{19}$ which displays the prototypical Schottky signature of a 2-level system. Along with the experimental data, a two-level Schottky fit, $C_m = p \cdot R \left(\frac{\Delta}{k_B T} \right)^2 \frac{\exp(\Delta/k_B T)}{[1 + \exp(\Delta/k_B T)]^2}$, where R is the ideal gas constant, Δ is the gap between the two levels, k_B is the Boltzmann's constant, and p represents the fraction of free ions²³ is depicted. In polycrystalline $\text{PrZnAl}_{11}\text{O}_{19}$, the C_m follows a power law in the temperature range between 0.2 and 2 K¹³. However in our $\text{PrMgAl}_{11}\text{O}_{19}$ data (Fig. 4(b)), C_m decreases faster than anticipated by a power law, suggesting the presence of a gap not seen in the Zn-analogue. On the other hand, the released entropy increases monotonically with increasing temperature, as shown in Fig. 4(c), in a similar manner to that seen in the polycrystalline $\text{PrZnAl}_{11}\text{O}_{19}$ sample¹³.

3 Discussions

One essential discovery in the present study is the quenched disorder observed from single crystal X-ray diffraction refinements. The role of disorder in QSL is still elusive, and varies significantly from sample to sample. While it may drive a system into a glassy state, it may also enhance quantum fluctuations and potentially facilitate the formation of a QSL state, as demonstrated both theoretically and experimentally^{3-5,24}. The AC susceptibility data in Fig. 3(c) and the lack of frequency-dependent in the data down to 50 mK, indicate that the system is still dynamic even though there is measurable site disorder. One possible scenario is the strong fluctuations resulting from the geometric frustration of antiferromagnetically coupled, easy-axis spins on the triangular lattice cannot be relieved by the site disorder ($\sim 7\%$), which would intuitively result in the destruction of the spin liquid state. Alternatively, the site disorder may cooperate with the frustration and stabilize a spin-liquid-like state as proposed for YbMgGaO_4 ^{2,25-29}. The present study does not have sufficient information to distinguish between these possibilities. Systematic studies on samples with different degrees of disorder will be instructive to clarify this point. Similar questions have been addressed in the pyrochlore oxide $\text{Yb}_2\text{Ti}_2\text{O}_7$, where a sharp peak in the specific heat for polycrystalline samples, due to a magnetic transition at ~ 265 mK³⁰, was not observed in many single crystals, where only a broad peak at lower temperature was observed^{31,32}. To investigate the small degree of site disorder found here within powder samples will need higher spatial resolution measurements, such as neutron/X-ray pair distribution function (PDF) method and extended X-ray absorption fine structure (EXAFS) to illustrate the local structure differences.

Another prominent feature of $\text{PrMgAl}_{11}\text{O}_{19}$ is the distinct Ising anisotropy revealed by the magnetization measurements. While the Heisenberg model usually predicts a magnetically ordered state for a triangular antiferromagnet, the Ising model can result in a macroscopically degenerated spin liquid state³³. Recent examples illustrating this concept is the TmMgGaO_4 ³⁴⁻³⁶ and neodymium heptatantalate, $\text{NdTa}_7\text{O}_{19}$ ³⁷. However, TmMgGaO_4 shows a partial order state below 0.7 K, and a lack of single crystals for $\text{NdTa}_7\text{O}_{19}$ hinders further explorations such as inelastic neutron scattering, as well as the exotic magnetic behaviors related to the crystalline directions. In this sense, the availability of large single crystals for $\text{PrMgAl}_{11}\text{O}_{19}$ provides a promising opportunity to investigate the triangular Ising model in depth.

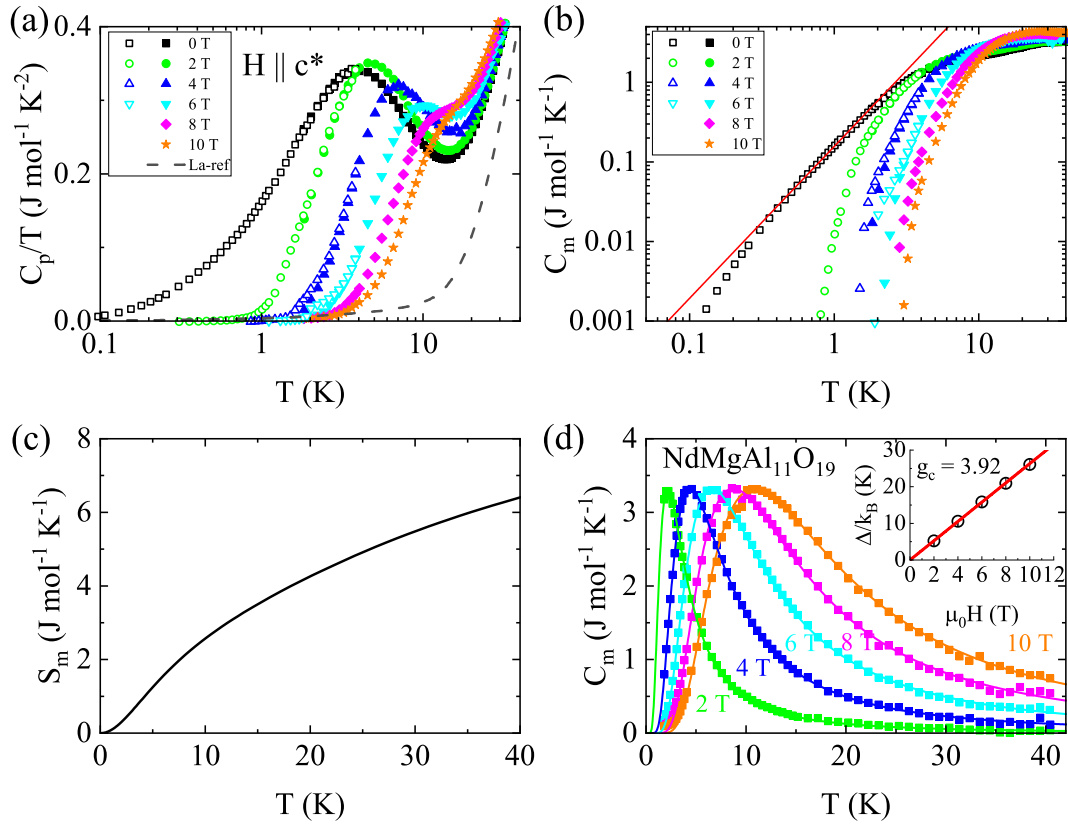


Figure 4. Heat capacity from hexaaluminate single crystals. (a) C_p/T versus T measured under various magnetic fields. The dashed line represents the phonon contribution obtained from the nonmagnetic counterpart LaMgAl₁₁O₁₉. (b) The magnetic specific heat is obtained by subtracting the phonon contributions (LaMgAl₁₁O₁₉) from the data of PrMgAl₁₁O₁₉. The red line represents a fit, $C_m = AT^\alpha$, to the zero field data in the temperature range between 0.2 and 2 K, with $\alpha = 1.91(1)$. (c) Representative change of the magnetic entropy in zero field. (d) Temperature dependence of the magnetic specific heat for NdMgAl₁₁O₁₉ together with a two-level Schottky fit. The inset shows the evolution of the gap as a function of the applied magnetic fields. A fit of $\Delta = g_c \mu_B H$ to the gap yields g_c of 3.92.

4 Conclusions

In summary, we have successfully synthesized centimeter-sized single crystals of a spin liquid candidate $\text{PrMgAl}_{11}\text{O}_{19}$ by means of the optical floating zone technique. Single crystal structure refinement unveiled the presence of about 7% quenched disorder at the Pr site in our sample. Directional magnetization measurements show a well-defined out-of-plane Ising anisotropy, which can induce strong fluctuations at a triangular lattice, as confirmed by the ac susceptibility measurements down to 50 mK. The availability of single crystals for this compound paves the way to explore the exotic magnetic properties by means of neutron scattering in the future.

While under review we became aware of a parallel work by Z. Ma *et al.*, who also conclude this sample is an Ising spin on the triangular lattice³⁸. Here, by combining the CEF calculation, magnetization data and estimated g -factors by ESR results, we present more robust evidence on the Ising anisotropy. Moreover, without single crystal structure refinement, the disorder at the Pr site was not reported in that work.

5 Future Perspectives

While disorder or defect is inevitable in real materials, many researchers endeavour to produce crystals as perfect as possible to obtain their intrinsic properties, allowing one to validate theoretical models. On the other hand, in recent years, it has been realized that disorder may result in exotic phases such spin-liquid-like random-singlet state. Unveiling the role of disorder systematically turns out to be as challenging as producing ideal crystals. In the title compound, the site disorder is within the triangular magnetic sublattice, which is unique compared to, e.g. YbMgGaO_4 where the site disorder occurs completely at the nonmagnetic site. By substituting Pr with another rare earth element, we expect to find evidence of different degrees of site disorder at the magnetic site (presumably this is also true when the nonmagnetic ions are substituted too), which will be helpful in future studies to manipulate the disorder in a controllable way. Substituting the rare-earth ion will also change the local spin character decorating the triangular lattice due to a change in the crystalline electric field scheme. This provides researchers with another tuning parameter for the magnetism in these hexaaluminates and should result in the discovery of systems with the spins confined to the triangular plane or with more exotic spin textures. As with the magnetic pyrochlore oxides³⁹, the availability of large single crystals and the large number of chemical substitutions that present themselves, we envisage this avenue of research to be very fruitful, resulting in materials with a variety of properties including superconductivity, emergent quantum phenomena, exotic spin texture and other quantum spin liquids.

6 Acknowledgments

This research was funded by the Guangdong Basic and Applied Basic Research Foundation (Grant No. 2022B1515120020), and the NSF of China with Grant No. 12004270 and 11874158. A portion of this work was performed on the Steady High Magnetic Field Facilities, High Magnetic Field Laboratory, CAS. A portion of this work was supported by the Laboratory Directed Research and Development (LDRD) program of Oak Ridge National Laboratory, managed by UT-Battelle, LLC for the U.S. Department of Energy.

7 Author contributions

Conceptualization: H.G., Z.T.; crystal growth: Y.C. and H.G.; measurement: Y.C., H.B., Z.T. and Z.O.; analysis: Y.C. and H.G.; validation: Z.F., J.S.G., Z.L., and J.Z.; writing: J.S.G. Z.T. and H.G. with inputs from all authors. All authors have read and agreed to the published version of the manuscript.

8 Conflict of interest

The authors declare no conflict of interests.

References

1. Balents, L. Spin liquids in frustrated magnets. *Nature* **464**, 199, DOI: [10.1038/nature08917](https://doi.org/10.1038/nature08917) (2010).
2. Ma, Z. *et al.* Spin-glass ground state in a triangular-lattice compound YbZnGaO_4 . *Phys. Rev. Lett.* **120**, 087201, DOI: [10.1103/PhysRevLett.120.087201](https://doi.org/10.1103/PhysRevLett.120.087201) (2018).
3. Savary, L. & Balents, L. Disorder-induced quantum spin liquid in spin ice pyrochlores. *Phys. Rev. Lett.* **118**, 087203, DOI: [10.1103/PhysRevLett.118.087203](https://doi.org/10.1103/PhysRevLett.118.087203) (2017).
4. Wen, J.-J. *et al.* Disordered route to the coulomb quantum spin liquid: Random transverse fields on spin ice in $\text{Pr}_2\text{Zr}_2\text{O}_7$. *Phys. Rev. Lett.* **118**, 107206, DOI: [10.1103/PhysRevLett.118.107206](https://doi.org/10.1103/PhysRevLett.118.107206) (2017).

5. Murayama, H. *et al.* Effect of quenched disorder on the quantum spin liquid state of the triangular-lattice antiferromagnet 1T-TaS₂. *Phys. Rev. Res.* **2**, 013099, DOI: [10.1103/PhysRevResearch.2.013099](https://doi.org/10.1103/PhysRevResearch.2.013099) (2020).
6. Gao, Y. & Chen, G. Some experimental schemes to identify quantum spin liquids. *Chin. Phys. B* **29**, 097501, DOI: [10.1088/1674-1056/ab9df0](https://doi.org/10.1088/1674-1056/ab9df0) (2020).
7. Knolle, J. & Moessner, R. A field guide to spin liquids. *Annu. Rev. Condens. Matter Phys.* **10**, 451–472, DOI: [10.1146/annurev-conmatphys-031218-013401](https://doi.org/10.1146/annurev-conmatphys-031218-013401) (2019).
8. Yamashita, M. *et al.* Highly mobile gapless excitations in a two-dimensional candidate quantum spin liquid. *Science* **328**, 1246–1248, DOI: [10.1126/science.1188200](https://doi.org/10.1126/science.1188200) (2010).
9. Ni, J. M. *et al.* Absence of magnetic thermal conductivity in the quantum spin liquid candidate EtMe₃Sb[Pd(dmit)₂]₂. *Phys. Rev. Lett.* **123**, 247204, DOI: [10.1103/PhysRevLett.123.247204](https://doi.org/10.1103/PhysRevLett.123.247204) (2019).
10. Saber, D., Dexpert-Ghys, J., Caro, P., Lejus, A. M. & Vivien, D. Analysis and simulation of optical and magnetic properties of lanthanide aluminates LnMgAl₁₁O₁₉ (Ln=La/Nd,La/Eu,Pr) with magnetoplumbite-like structure. *J. Chem. Phys.* **82**, 5648–5657, DOI: [10.1063/1.448551](https://doi.org/10.1063/1.448551) (1985).
11. Kahn, A. *et al.* Preparation, structure, optical, and magnetic properties of lanthanide aluminate single crystals (LnMAl₁₁O₁₉). *J. Appl. Phys.* **52**, 6864–6869, DOI: [10.1063/1.328680](https://doi.org/10.1063/1.328680) (1981).
12. Ashtar, M. *et al.* REZnAl₁₁O₁₉ (RE = Pr, Nd, Sm - Tb): a new family of ideal 2d triangular lattice frustrated magnets. *J. Mater. Chem. C* **7**, 10073–10081, DOI: [10.1039/C9TC02643F](https://doi.org/10.1039/C9TC02643F) (2019).
13. Bu, H. *et al.* Gapless triangular-lattice spin-liquid candidate PrZnAl₁₁O₁₉. *Phys. Rev. B* **106**, 134428, DOI: [10.1103/PhysRevB.106.134428](https://doi.org/10.1103/PhysRevB.106.134428) (2022).
14. Li, Y. YbMgGaO₄: A triangular-lattice quantum spin liquid candidate. *Adv. Quantum Techno.* **2**, 1900089, DOI: <https://doi.org/10.1002/qute.201900089> (2019).
15. Petříček, V., Dušek, M. & Palatinus, L. Crystallographic computing system JANA2006: General features. *Z. Kristallogr.* **229**, 345–352, DOI: [doi:10.1515/zkri-2014-1737](https://doi.org/10.1515/zkri-2014-1737) (2014).
16. Rodríguez-Carvajal, J. Recent advances in magnetic structure determination by neutron powder diffraction. *Phys. B* **192**, 55–69, DOI: [http://dx.doi.org/10.1016/0921-4526\(93\)90108-I](https://doi.org/10.1016/0921-4526(93)90108-I) (1993).
17. See the “Supplementary Materials”.
18. Cao, Y., Pomjakushin, V., Gardner, J. S. & Guo, H. Data to be published.
19. Scheie, A. *PyCrystalField*: software for calculation, analysis and fitting of crystal electric field Hamiltonians. *J. Appl. Cryst.* **54**, 356–362, DOI: [10.1107/S160057672001554X](https://doi.org/10.1107/S160057672001554X) (2021).
20. Scheie, A., Garlea, V. O., Sanjeeva, L. D., Xing, J. & Sefat, A. S. Crystal-field hamiltonian and anisotropy in KErSe₂ and CsErSe₂. *Phys. Rev. B* **101**, 144432, DOI: [10.1103/PhysRevB.101.144432](https://doi.org/10.1103/PhysRevB.101.144432) (2020).
21. Schotte, K. D. & Schotte, U. Interpretation of kondo experiments in a magnetic field. *Phys. Lett. A* **55**, 38–40, DOI: [https://doi.org/10.1016/0375-9601\(75\)90386-2](https://doi.org/10.1016/0375-9601(75)90386-2) (1975).
22. Bredl, C. D., Steglich, F. & Schotte, K. D. Specific heat of concentrated kondo systems: (La, Ce)Al₂ and CeAl₂. *Z. Phys. B* **29**, 327–340, DOI: [10.1007/BF01324030](https://doi.org/10.1007/BF01324030) (1978).
23. Gopal, E. *Specific Heats At Low Temperatures* (Plenum Press, 1966).
24. Furukawa, T. *et al.* Quantum spin liquid emerging from antiferromagnetic order by introducing disorder. *Phys. Rev. Lett.* **115**, 077001, DOI: [10.1103/PhysRevLett.115.077001](https://doi.org/10.1103/PhysRevLett.115.077001) (2015).
25. Kimchi, I., Nahum, A. & Senthil, T. Valence bonds in random quantum magnets: Theory and application to YbMgGaO₄. *Phys. Rev. X* **8**, 031028, DOI: [10.1103/PhysRevX.8.031028](https://doi.org/10.1103/PhysRevX.8.031028) (2018).
26. Li, Y. *et al.* Rearrangement of uncorrelated valence bonds evidenced by low-energy spin excitations in YbMgGaO₄. *Phys. Rev. Lett.* **122**, 137201, DOI: [10.1103/PhysRevLett.122.137201](https://doi.org/10.1103/PhysRevLett.122.137201) (2019).
27. Wu, H.-Q., Gong, S.-S. & Sheng, D. N. Randomness-induced spin-liquid-like phase in the spin- $\frac{1}{2}$ $J_1 - J_2$ triangular heisenberg model. *Phys. Rev. B* **99**, 085141, DOI: [10.1103/PhysRevB.99.085141](https://doi.org/10.1103/PhysRevB.99.085141) (2019).
28. Ma, Z. *et al.* Disorder-induced broadening of the spin waves in the triangular-lattice quantum spin liquid candidate YbZnGaO₄. *Phys. Rev. B* **104**, 224433, DOI: [10.1103/PhysRevB.104.224433](https://doi.org/10.1103/PhysRevB.104.224433) (2021).
29. Li, Y., Gegenwart, P. & Tsirlin, A. A. Spin liquids in geometrically perfect triangular antiferromagnets. *J. Phys.: Condens. Matter* **32**, 224004, DOI: [10.1088/1361-648X/ab724e](https://doi.org/10.1088/1361-648X/ab724e) (2020).

30. Hodges, J. A. *et al.* First-order transition in the spin dynamics of geometrically frustrated $\text{Yb}_2\text{Ti}_2\text{O}_7$. *Phys. Rev. Lett.* **88**, 077204, DOI: [10.1103/PhysRevLett.88.077204](https://doi.org/10.1103/PhysRevLett.88.077204) (2002).
31. Yaouanc, A., Dalmas de Réotier, P., Marin, C. & Glazkov, V. Single-crystal versus polycrystalline samples of magnetically frustrated $\text{Yb}_2\text{Ti}_2\text{O}_7$: Specific heat results. *Phys. Rev. B* **84**, 172408, DOI: [10.1103/PhysRevB.84.172408](https://doi.org/10.1103/PhysRevB.84.172408) (2011).
32. Ross, K. A. *et al.* Lightly stuffed pyrochlore structure of single-crystalline $\text{Yb}_2\text{Ti}_2\text{O}_7$ grown by the optical floating zone technique. *Phys. Rev. B* **86**, 174424, DOI: [10.1103/PhysRevB.86.174424](https://doi.org/10.1103/PhysRevB.86.174424) (2012).
33. Wannier, G. H. Antiferromagnetism. the triangular ising net. *Phys. Rev.* **79**, 357–364, DOI: [10.1103/PhysRev.79.357](https://doi.org/10.1103/PhysRev.79.357) (1950).
34. Shen, Y. *et al.* Intertwined dipolar and multipolar order in the triangular-lattice magnet TmMgGaO_4 . *Nat. Commun.* **10**, 4530, DOI: [10.1038/s41467-019-12410-3](https://doi.org/10.1038/s41467-019-12410-3) (2019).
35. Li, Y. *et al.* Partial up-up-down order with the continuously distributed order parameter in the triangular antiferromagnet TmMgGaO_4 . *Phys. Rev. X* **10**, 011007, DOI: [10.1103/PhysRevX.10.011007](https://doi.org/10.1103/PhysRevX.10.011007) (2020).
36. Li, H. *et al.* Kosterlitz-thouless melting of magnetic order in the triangular quantum ising material TmMgGaO_4 . *Nat. Commun.* **11**, 1111, DOI: [10.1038/s41467-020-14907-8](https://doi.org/10.1038/s41467-020-14907-8) (2020).
37. Arh, T. *et al.* The Ising triangular-lattice antiferromagnet neodymium heptatantalate as a quantum spin liquid candidate. *Nat. Mater.* **21**, 416–422, DOI: [10.1038/s41563-021-01169-y](https://doi.org/10.1038/s41563-021-01169-y) (2022).
38. Ma, Z. *et al.* Possible gapless quantum spin liquid behavior in the triangular-lattice ising antiferromagnet $\text{PrMgAl}_{11}\text{O}_{19}$. *Phys. Rev. B* **109**, 165143, DOI: [10.1103/PhysRevB.109.165143](https://doi.org/10.1103/PhysRevB.109.165143) (2024).
39. Gardner, J. S., Gingras, M. J. P. & Greedan, J. E. Magnetic pyrochlore oxides. *Rev. Mod. Phys.* **82**, 53–107 (2010).
40. Bianconi, A. *et al.* Many-body effects in praseodymium core-level spectroscopies of PrO_2 . *Phys. Rev. B* **38**, 3433–3437, DOI: [10.1103/PhysRevB.38.3433](https://doi.org/10.1103/PhysRevB.38.3433) (1988).
41. Ogasawara, H., Kotani, A., Potze, R., Sawatzky, G. A. & Thole, B. T. Praseodymium 3d- and 4d-core photoemission spectra of Pr_2O_3 . *Phys. Rev. B* **44**, 5465–5469, DOI: [10.1103/PhysRevB.44.5465](https://doi.org/10.1103/PhysRevB.44.5465) (1991).
42. Holland-Moritz, E. Coexistence of valence fluctuating and stable pr ions in Pr_6O_{11} . *Z. Phys. B: Condens. Matter* **89**, 285–288 (1992).
43. Gurgul, J., Rinke, M. T., Schellenberg, I. & Pöttgen, R. The antimonide oxides ReZnSbO and ReMnSbO (re= ce, pr)—an xps study. *Solid State Sci.* **17**, 122–127 (2013).
44. Lütkehoff, S., Neumann, M. & Ślebarski, A. 3d and 4d x-ray-photoelectron spectra of pr under gradual oxidation. *Phys. Rev. B* **52**, 13808–13811, DOI: [10.1103/PhysRevB.52.13808](https://doi.org/10.1103/PhysRevB.52.13808) (1995).
45. Wen, J.-J. *et al.* Disordered route to the coulomb quantum spin liquid: Random transverse fields on spin ice in $\text{Pr}_2\text{Zr}_2\text{O}_7$. *Phys. Rev. Lett.* **118**, 107206, DOI: [10.1103/PhysRevLett.118.107206](https://doi.org/10.1103/PhysRevLett.118.107206) (2017).
46. Li, Y., Bachus, S., Tokiwa, Y., Tsirlin, A. A. & Gegenwart, P. Gapped ground state in the zigzag pseudospin-1/2 quantum antiferromagnetic chain compound PrTiNbO_6 . *Phys. Rev. B* **97**, 184434, DOI: [10.1103/PhysRevB.97.184434](https://doi.org/10.1103/PhysRevB.97.184434) (2018).
47. Chen, G. Intrinsic transverse field in frustrated quantum ising magnets: Physical origin and quantum effects. *Phys. Rev. Res.* **1**, 033141, DOI: [10.1103/PhysRevResearch.1.033141](https://doi.org/10.1103/PhysRevResearch.1.033141) (2019).

9 Supplementary Materials

9.1 Powder X-ray diffraction

The powder X-ray diffraction pattern for the crushed single crystals is shown in Fig. S1. Due to the strong preferred orientation related to the two-dimensional character of the sample, the final agreement factors are relatively high even when the preferred orientation was considered during the refinement using the Fullprof package. However, the key information is that no additional peaks were observed from this measurement, indicating an impurity-free phase within our experimental resolution.

9.2 X-ray Photoelectron Spectroscopy

Due to the fact that Pr ion can display different valence states in oxides, we performed X-ray photoelectron spectroscopy (XPS) measurements to investigate the valence of Pr in our single crystals. The measurements were carried out on an XPS spectrometer (Thermo Fisher ESCALAB XI+) equipped with a monochromated $\text{Al } K_\alpha$ X-ray source. The spectra are fitted using the Avantage software.

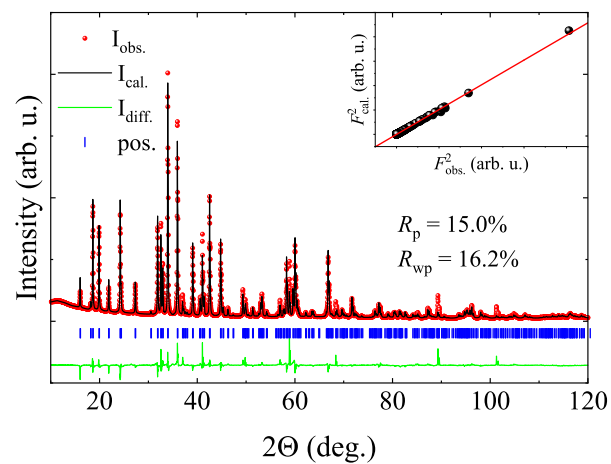


Figure S1. Rietveld refinement of the powder X-ray diffraction pattern for $\text{PrMgAl}_{11}\text{O}_{19}$. The inset shows the $F_{\text{obs.}}^2$ vs. $F_{\text{cal.}}^2$ from single crystal refinement. The straight line is a guide to the eye.

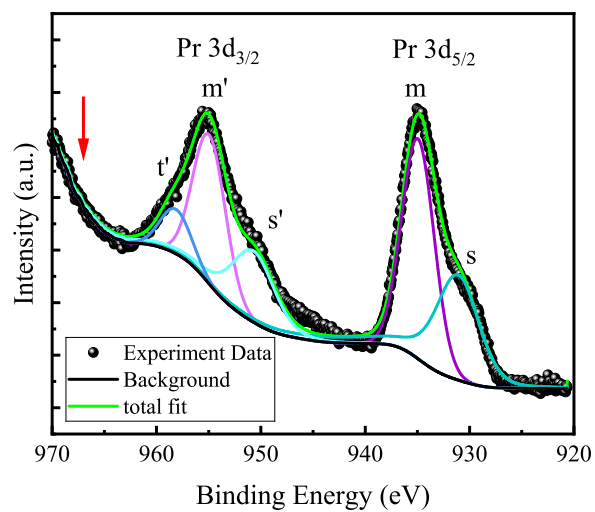


Figure S2. Pr 3d X-ray photoelectron spectroscopy for $\text{PrMgAl}_{11}\text{O}_{19}$ single crystal. The red arrow indicates the expected peak position for the Pr^{4+} state.

Table 3. CEF eigenvectors and eigenvalues for Pr^{3+} at the $2d$ site.

E (meV)	$ -4\rangle$	$ -3\rangle$	$ -2\rangle$	$ -1\rangle$	$ 0\rangle$	$ 1\rangle$	$ 2\rangle$	$ 3\rangle$	$ 4\rangle$
0.000	-0.9588	0.0	0.0	0.0	0.0	0.0	-0.2842	0.0	0.0
0.000	0.0	0.0	-0.2842	0.0	0.0	0.0	0.0	0.0	-0.9588
19.949	0.0	0.7071	0.0	0.0	0.0	0.0	0.0	0.7071	0.0
42.086	-0.2842	0.0	0.0	0.0	0.0	0.0	0.9588	0.0	0.0
42.086	0.0	0.0	-0.9588	0.0	0.0	0.0	0.0	0.0	0.2842
43.287	0.0	0.0	0.0	-1.0	0.0	0.0	0.0	0.0	0.0
43.287	0.0	0.0	0.0	0.0	0.0	-1.0	0.0	0.0	0.0
46.241	0.0	0.0	0.0	0.0	-1.0	0.0	0.0	0.0	0.0
50.291	0.0	-0.7071	0.0	0.0	0.0	0.0	0.0	0.7071	0.0

Previous studies have demonstrated that Pr $3d$ XPS can clearly distinguish between Pr^{4+} and Pr^{3+} ^{40–43}. As shown in Fig. S2, the spectrum exhibits two main peaks (m and m') which are due to the spin-orbit split $3d_{3/2}$ and $3d_{5/2}$ core holes. In addition, several satellites (s , s' and t') can be observed due to the multiplet effect. All these features are reminiscent of the results for Pr_2O_3 ⁴⁴. Moreover, no marker peak for Pr^{4+} (~ 967.0 eV) was observed. Thus, we can safely conclude that a Pr^{3+} state is formed in our single crystal.

9.3 Electron spin resonance

The high-field electron spin resonance (ESR) spectra were collected in the field-increasing process in a frequency range of 60 to 154 GHz at Wuhan National High Magnetic Field Centre (WHMFC). The resonance line of standard sample DPPH with $g = 2.0$ was used for a field marker. The absorption spectra measured at different frequencies are shown in Fig. S3(a), from which the resonant field, H_r , can be identified. As can be seen from Fig. S3(b), the absorption becomes more and more indiscernible at high temperatures, suggesting that we are probing the ground state. Moreover, as shown in Fig. S3(c), the absorption frequency depends linearly on H_r such that $f = f_0 + g_c \mu_B \mu_0 H_r / h$, where μ_B is the Bohr magneton, h is the Planck constant. The best fit yields the g_c value of 5.1 and f_0 of 26.2 GHz. The nonzero f_0 indicates the presence of a zero-field gap of ~ 0.1 meV.

9.4 Crystal-electric-field analyses

As described in the main text, the CEF eigenvalues and eigenvectors extracted from the fitting to the $\chi_c^{-1}(T)$ data are shown in Tab. 3. The calculated g_c from the ground state doublet amounts to 5.6, which is consistent with the ESR measurement. Since Pr^{3+} is a non-Kramers ion, the ground state doublet is not protected by the time reversal symmetry, and can be split by further lattice distortions, which is plausible regarding the site disorder at the Pr site. The zero field splitting observed by ESR supports this speculation. However, the splitting is very small (~ 0.1 meV), the ground state can still be viewed as a quasidoublet, as observed in many related non-Kramers systems^{45,46}. In this case, the longitudinal spin component behaves as the magnetic dipole moment, while the transverse component like multipoles^{34,47}.

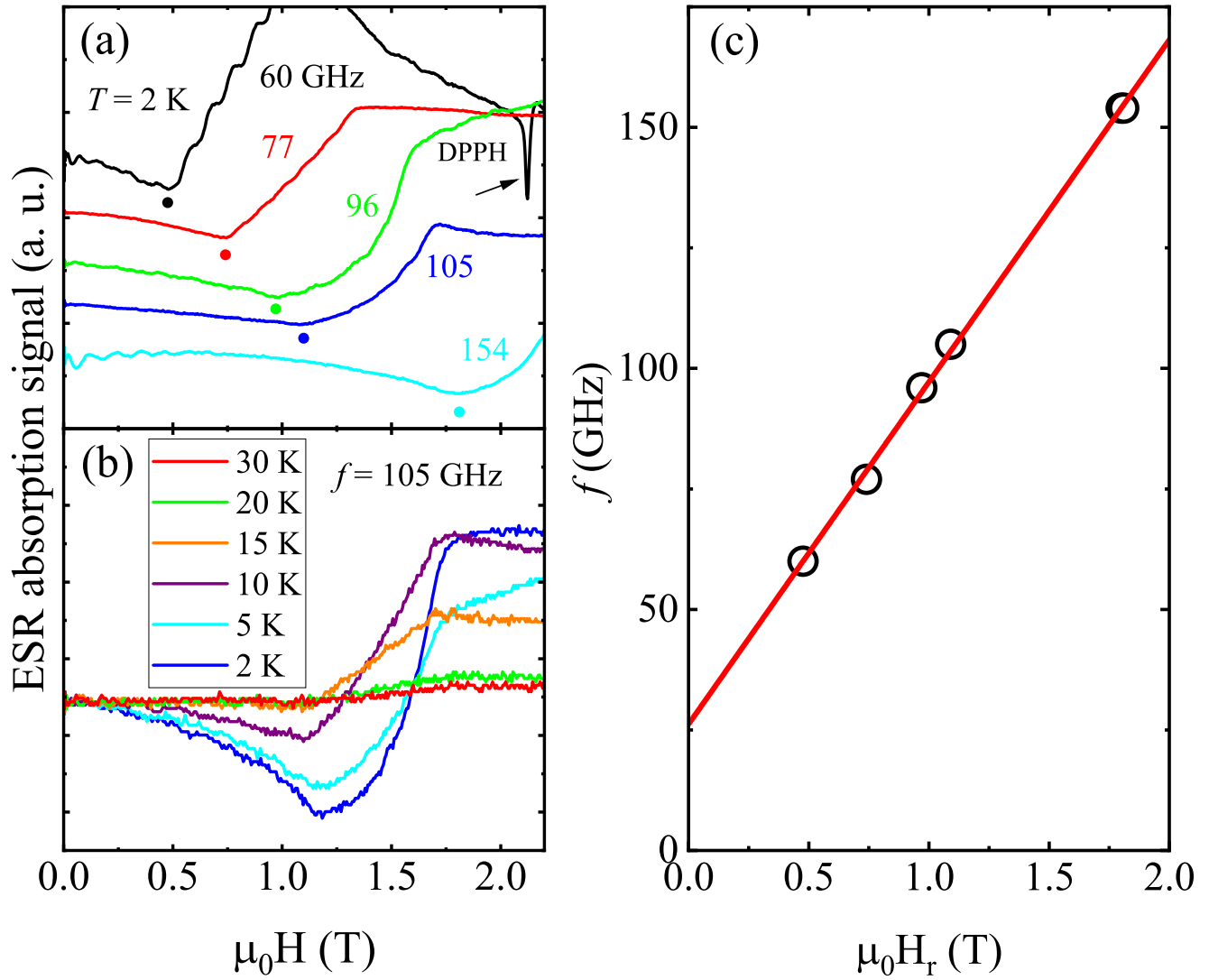


Figure S3. (a) Electron spin resonance spectroscopy for $\text{PrMgAl}_{11}\text{O}_{19}$ measured at 2 K with magnetic field applied along the c axis. The small dots under each line indicate the resonant field H_r positions. (b) The $f = 105$ GHz spectra measured at various temperatures. (c) Magnetic field dependence of the ESR absorption frequency. The red line is a linear fit, see the text for details.